Asymmetric internal tide generation in the presence of a steady flow

Yvan Dossmann[1,2], Callum Shakespeare[2], Kial Stewart[2], Andrew McC. Hogg[2,3]

Corresponding author: Yvan Dossmann, LEMTA, Université de Lorraine, CNRS, France. (yvan.dossmann@univ-lorraine.fr)

[1]LEMTA, UMR 7563, Université de Lorraine, CNRS, F-54500 Vandoeuvre-les-Nancy, France

[2]Research School of Earth Sciences, The Australian National University, Canberra 2601, Australia

[3]ARC Centre of Excellence for Climate Extremes

Key Points.

- The dynamics of topographic internal waves generated by the sum of a steady and oscillatory flow is studied for varying ridge shape.
- A topographically controlled asymmetry is measured in the energy fluxes carried by the upstream and downstream IW beams.
- The asymmetry and the generation of nonlinear structures impact the distribution of IW induced mixing in the ocean interior.

Abstract.

The generation of topographic internal waves (IWs) by the sum of an oscillatory and a steady flow is investigated experimentally and with a linear model. The two forcing flows represent the combination of a tidal constituent and a weaker quasi-steady flow interacting with an abyssal hill. The combined forcings cause a coupling between internal tides and lee waves that impacts their dynamics of internal waves as well as the energy carried away. An asymmetry is observed in the structure of upstream and downstream internal wave beams due to a Doppler shift effect. This asymmetry is enhanced for the narrowest ridge on which a super-buoyancy ($\omega > N$) downstream beam and an evanescent upstream beam are measured.

Energy fluxes are measured and compared with the linear model, that has been extended to account for the coupling mechanism. The structure and amplitude of energy fluxes match well in most regimes, showing the relevance of the linear prediction for IW wave energy budgets, while the energy flux toward IW beams is limited by the generation of periodic vortices in a particular experiment. The upstream-bias energy flux - and consequently net

horizontal momentum - described in *Shakespeare* [2020] is measured in the experiments.

The coupling mechanism plays an important role in the pathway to IW induced mixing, that has previously been quantified independently for lee waves and internal tides. Hence, future parameterizations of IW processes ought to include the coupling mechanism to quantify its impact on the global distribution of mixing.

Plain language summary

When tides and currents interact with abyssal topographies, such as ridges and hills, they generate internal waves that propagate in the ocean interior. The energy transported by these waves sustains the largest scale oceanic motions. To improve our understanding of how and where energy is transferred to oceanic currents, an important step is to describe the fate of internal waves, from their generation to their breaking.

Previous studies have independently described the dynamics of internal waves generated by tides, or by a steady current. Here we combine the two types of currents - a situation that is met at many oceanic sites - using laboratory experiments and a linear model. The combined currents cause an asymmetry in the internal wave structure. Internal waves are more energetic on the upstream side of the ridge, a phenomenon that is amplified when decreasing the ridge width. The measured energy matches the model prediction in all but one experiment. This gap is likely related to the formation of a vertical swirl close to the ridge that limits energy transfers to internal waves.

These results contributes to improve our understanding of the internal wave dynamics and to better represent their effects in oceanic models.

1. Introduction

Internal waves play an important role in sustaining the Meridional Overturning Circulation (MOC) by inducing a wide range of turbulent mixing processes [*Sarkar and Scotti*, 2017; *MacKinnon et al.*, 2017]. Internal waves are predominantly generated either at the surface by wind fluctuations or at the ocean bottom by the interaction of flow with topography. Two seemingly independent classes of topographic internal waves have been distinguished in previous studies. In regions where strong barotropic tidal flows interact

with large scale topographies, such as the Mid-Atlantic Ridge, internal waves are usually organized as propagating beams called internal tides [*Polzin et al.*, 1997; *Gregg and Ozsoy*, 1999; *Melet et al.*, 2013a; *Nycander*, 2005, 2006; *Buijsman et al.*, 2014]. On the other hand, in regions where a vigorous geostrophic eddy fields interact with smaller scale topographies such as in the Antarctic Circumpolar Current, internal waves are organized as quasi-steady lee waves [*Nikurashin and Ferrari*, 2010a, b; *Dossmann et al.*, 2016a; *Yang et al.*, 2018; *Zheng and Nikurashin*, 2019]. The respective contributions of these two classes of internal waves to water-masses transformation have been assessed independently using the linear theory of *Bell* [1975] and semi-empirical parameterizations [*St. Laurent et al.*, 2002; *Polzin*, 2009] leading to global estimates maps of internal wave mixing (e.g. *Nikurashin and Ferrari* [2011, 2013]; *Melet et al.* [2013b]).

Barotropic tides coexist with quasi-steady flows at many internal wave generation sites. This observation motivated *Shakespeare* [2020] to revisit the classical linear internal wave generation theory of *Bell* [1975]. The combination of a barotropic tidal component and a steady flow causes a linear coupling between internal tides and lee waves that has not been accounted for in previous internal wave energy budgets. *Bell* [1975]'s theory was extended to include the coupling between multiple flow constituents. A new nomenclature was introduced to distinguish internal waves propagating as 'free beams' from 'flow-trapped' waves that can only propagate in the presence of the flow that supports them.

The extended linear theory predicts major changes in the internal wave dynamics owing to this coupling that affects:

• The energy fluxes to lee waves. Lee wave generation and induced mixing are largely cancelled (by up to 90%- in some key areas, such as the Drake Passage) and is overestimated by $13-19\%$ on a global scale using the classical approach.

• The generation of internal tides beyond the critical latitudes. Doppler-shifted internal wave beams can propagate in regions where they would dissipate in the absence of a steady flow, hence modifying the spatical distribution of internal waves and subsequent mixing.

• The existence of a net wave stress above abyssal hills. The linear coupling causes an asymmetry between the upstream and downstream internal tide beams generated over hills, which induces a net wave stress of $0.01-0.1$ N/m^2 (comparable to the local wind stress).

Several limitations have been put forward by *Shakespeare* [2020] regarding the application of the classical and extended theory of *Bell* [1975]. First, the model is linear and does not account for finite amplitude effects that induce flow blocking and saturation in the supercritical regime. Second, the large uncertainties on the deep-ocean stratification and geostrophic flows lead to an important variability of internal wave energy, momentum and mixing budgets between studies.

The use of laboratory experiments permits exploration of the dynamics of internal waves and the pathway to mixing in controlled parameter ranges that are relevant to real oceanic processes [*Aguilar et al.*, 2006; *Zhang et al.*, 2007; *Bourget et al.*, 2013; *Dossmann et al.*, 2011, 2016b]. The turbulent regime is sufficient for the development of nonlinear processes leading to the direct cascade to mixing scales. In a previous experimental study, both the linear lee wave field predicted by Bell's theory and a complex nonlinear dynamics in the boundary layer were captured using the light attenuation technique [*Dossmann et al.*,

92 2016a]. Mixing diagnostics were performed and showed that the nonlinear processes close
93 to the topography overcome internal wave induced mixing in ocean relevant parameter
94 regimes, highlighting the need to account for these effects in the mass and energy budgets
95 of the Meridional Overturning Circulation [*Todd*, 2017; *MacKinnon et al.*, 2017; *Zheng*
96 *and Nikurashin*, 2019].

97 The present work aims to describe the linear dynamics of topographic internal waves
98 forced by the combination of an oscillatory flow and a steady flow, and to accurately
99 quantify the associated energy flux. It relies on an experimental campaign for which the
100 flow, topography and background stratification are precisely controlled and the flow dy-
101 namics is measured at high space-time resolution. This idealized approach permits direct
102 comparison of the linear energy flux estimated from the extended theory of *Bell* [1975]
103 against measurements in an identical configuration, allowing the generation of internal
104 waves as well as non-linear structures that also participate to mixing.

105 The manuscript is organized as follows. In section 2, the extended linear theory is
106 described and the different internal wave regimes are introduced. The experimental setup
107 is presented in section 3. The internal wave dynamics and energy flux fields are described
108 in sections 4 and 5. Implications for IW energy budgets in the ocean are discussed in
109 section 6.

2. Linear theory

2.1. Extended linear theory

110 In order to make meaningful comparisons with our experimental results, it is necessary
111 to slightly extend previous models for linear internal wave generation by flow over topog-
112 raphy to simultaneously include: (i) finite fluid depth, (ii) both steady and oscillatory

background flow, (iii) non-negligible excursion parameters, (iv) non-hydrostatic dynamics, and (v) a mechanism of dissipation for the waves. As such, the theory here can be thought of as generalising that of *Bell* [1975] and *Shakespeare* [2020] to include finite-depth and wave dissipation, or the theory of *Shakespeare et al.* [2020a] to include non-negligible excursion parameters.

Here, the background flow of interest is a combined steady and oscillatory flow: $\boldsymbol{U} = \boldsymbol{U}_c + \boldsymbol{U_0}\cos\omega t$, where ω is the forcing frequency and t is time. For completeness, we will include a non-zero Coriolis parameter f and three-dimensionality in the following. The simplest starting point for our derivation is Equation (21)-(25) in *Shakespeare et al.* [2020a] which describes the vertical velocity $w(x,y,z,t)$ and pressure $p(x,y,z,t)$ associated with wave generation at the ocean bottom ($z=-H$) and a rigid-lid boundary condition at the ocean surface ($z=0$):

$$\widehat{w}_n = \widehat{w}_n|_{-H}\frac{e^{-imz-\gamma z} - e^{imz+\gamma z}}{e^{imH+\gamma H} - e^{-imH-\gamma H}}, \tag{1a}$$

and,

$$\widehat{p}_n = -\frac{N^2-\omega_n^2}{m\omega_n}\widehat{w}_n|_{-H}\frac{e^{-imz-\gamma z} + e^{imz+\gamma z}}{e^{imH+\gamma H} - e^{-imH-\gamma H}}, \tag{1b}$$

where

$$m = \mathrm{sgn}(\omega_n)K\sqrt{\frac{N^2-\omega_n^2}{\omega_n^2-f^2}}, \tag{1c}$$

is the vertical wavenumber, $K=\sqrt{k^2+l^2}$ is the horizontal wavenumber modulus, and

$$\gamma = \alpha m\frac{\omega_n(2N^2-\omega_n^2-f^2)}{2(N^2-\omega_n^2)(\omega_n^2-f^2)}, \tag{1d}$$

is the decay rate per unit wavelength, with $\gamma \ll m$ for valid solutions. The magnitude of this decay rate is determined by the Rayleigh drag α (in inverse seconds) — this damping

is used as a purely numerical tool herein, as will be explained below. Equation (1) may be generalised to include steady and tidal flows, and large excursion distances, by summing over intrinsic frequencies for each harmonic

$$\omega_n = n\omega + \boldsymbol{k} \cdot \boldsymbol{U}_c. \tag{2}$$

where n is the harmonic number, and the Fourier transform in x and y of the total vertical velocity is thus

$$\widehat{w}(k, l, z, t) = \sum_{n=-\infty}^{\infty} \widehat{w}_n \, e^{i\omega_n t}, \tag{3}$$

and similarly for pressure. The bottom boundary condition on the vertical velocity, associated with the no-normal flow condition (i.e. $w = \boldsymbol{U} \cdot \boldsymbol{\nabla} h$ for topographic height h in the small amplitude approximation) gives

$$\widehat{w}_n|_{-H} = i\omega_n \widehat{h} \, J_n \left(\frac{\boldsymbol{k} \cdot \boldsymbol{U}_0}{\omega} \right), \tag{4}$$

where J_n is the order n Bessel function of the first kind (see, for example, *Bell* [1975]; *Shakespeare* [2020]).

The solution in this form is expressed in a coordinate frame $\boldsymbol{x_0}$ *following the total flow* $\boldsymbol{U}$ (that is, $\boldsymbol{x} = \boldsymbol{x_0} + \int_0^t \boldsymbol{U} \, dt'$ where $\boldsymbol{x}$ is the Eulerian position, and $\boldsymbol{x_0}$ the flow-following coordinate). We use the above solutions to compute the theoretical energy flux as a function of time and space via

$$F(x, y, z, t) = \mathcal{F}^{-1}[\widehat{w} e^{-i\boldsymbol{k}\cdot\boldsymbol{U}_c t}] \mathcal{F}^{-1}[\widehat{p} e^{-i\boldsymbol{k}\cdot\boldsymbol{U}_c t}], \tag{5}$$

where $\mathcal{F}^{-1} = 1/(4\pi^2) \int\int e^{-i(kx+ly)} dk \, dl$ denotes the inverse Fourier transform. To calculate these inverse Fourier transforms numerically, the vertical velocity and pressure

fields must decay towards the boundaries of the (numerical) domain; otherwise, the waves continuously wrap around and the numerical solution is meaningless. The decay of the wave fields is ensured by turning the Rayleigh drag α in (1d) to a sensible value (interested readers are referred to *Shakespeare et al.* [2020b] for a discussion of the impact α on the wave field).

2.2. Internal wave regimes

Four internal wave regimes are expected due to the combination of a steady and an oscillatory forcing flow. The linearization of Euler's equation under the Boussinesq approximation leads to the following dispersion relation for internal waves:

$$\tilde{\omega}^2 = N^2 \sin\theta^2 + f^2 \cos\theta^2, \tag{6}$$

with $\tilde{\omega} = \omega - \boldsymbol{k} \cdot \boldsymbol{U_c}$, N and f the intrinsic internal wave frequency, the Brunt-Väisälä frequency and the local Coriolis parameter. Here, ω is the frequency of the oscillatory flow, $\boldsymbol{k} \cdot \boldsymbol{U_c}$ is a quasi Doppler frequency shift induced by the geostrophic flow $\boldsymbol{U_c}$ onto the internal wave of horizontal wavenumber $\boldsymbol{k}$, and θ is the angle of the group velocity with respect to the horizontal. Equation (6) implies that $f < |\tilde{\omega}| < N$ for propagating internal waves. Depending on the signs of $|\boldsymbol{k} \cdot \boldsymbol{U_c}|/\omega$ (the dot-product of the inverse wave phase speed and the steady flow velocity) and $\tilde{\omega}$ four non-evanescent bands are allowed: lee waves, upstream and downstream beams, and tidal lee waves. The four bands are represented in Fig. 1a. in the non-rotating case.

The first non-evanescent band, indicated by the solid red line in Fig. 1a. corresponds to the classical lee wave generation by the steady forcing ($\omega = 0$, $f < |\boldsymbol{k} \cdot \boldsymbol{U_c}| < N$) downstream of the steady flow.

There are two non-evanescent bands (blue shaded areas in Fig. 1a) with positive intrinsic frequencies $\tilde{\omega} > 0$, one in the upstream direction ($\boldsymbol{k} \cdot \boldsymbol{U_c}/\omega < 0$, $f - |\boldsymbol{k} \cdot \boldsymbol{U_c}| < \omega < N - |\boldsymbol{k} \cdot \boldsymbol{U_c}|$), and one in the downstream direction ($\boldsymbol{k} \cdot \boldsymbol{U_c}/\omega > 0$, $f + |\boldsymbol{k} \cdot \boldsymbol{U_c}| < \omega < N + |\boldsymbol{k} \cdot \boldsymbol{U_c}|$). In these two bands, the internal wave field is organized as beams propagating upstream and downstream of the flow. The dispersion relation for the downstream and upstream beams are shown in Figs 1b and c for the three experimental ridges. In particular internal waves are able to propagate in regions where $\omega > N$ (superbuoyancy downstream beam) or $\omega < f$ (subinertial upstream beam).

In the downstream direction, non-evanescent IWs with $\tilde{\omega} < 0$ are allowed in the band $|\boldsymbol{k} \cdot \boldsymbol{U_c}| - N < \omega < |\boldsymbol{k} \cdot \boldsymbol{U_c}| - f$ (red shaded areas in Fig. 1a). In this band, IWs are organized as a steady lee wave field at larger wavenumber than classical lee waves and which only exists in the presence of a barotropic forcing. The term tidal lee waves was introduced by *Shakespeare* [2020] to refer to this IW regime.

Three of the four internal wave regimes generated by the combination of a steady and an oscillatory flow are shown in Fig.2 using the extended linear model described in the previous section. The two forcing flows are artificially uncoupled in Fig.2a, in which one identifies the generation of symmetrical internal tidal beams on either side of the ridge as well as lee waves. Turning on the coupling leads to more complex dynamics. The symmetry between the upstream beam and the downstream beam is broken by the presence of the steady flow as will be discussed in section 4. Lee waves are still generated on the downstream side, but their amplitude is weakened by the coupling mechanism. For the chosen forcing parameters, the generation of tidal lee waves is limited by the relatively small value of the steady flow, as will be the case in the experiments.

In this work experiments are performed in a non-rotating, strongly stratified flow. The effects of rotation on the IW dynamics are neglected on the experiment timescale. The dispersion relation (6) can therefore be simplified to $\omega = N\sin(\theta) - |\boldsymbol{k}\cdot\boldsymbol{U_c}|$ for the upstream beam and $\omega = N\sin(\theta) + |\boldsymbol{k}\cdot\boldsymbol{U_c}|$ for the downstream beam, as shown in Fig. 1. The mean excursion distance parameter $\bar{\epsilon} = |\boldsymbol{k}\cdot\boldsymbol{U_c}|/\omega$ is introduced to quantify the relative magnitude of the quasi-Doppler shift, and hence the asymmetry between the upstream and downstream beams. The beam horizontal wavenumber is not prescribed by the dispersion relation, but scaled by the topographic width. Hence, the asymmetry between the upstream and downstream beams is expected to be enhanced for strong steady flows impinging on smaller scale topographies.

The experimental campaign aims to describe the internal wave field induced by the combined forcings and the effect of the asymmetry on the transported energy fluxes.

3. Experimental set-up

3.1. Apparatus

Experiments have been performed in a 5.26 m long, 20 cm wide and 40 cm high perspex tank in the Geophysical Fluid Dynamics laboratory at ANU. The air temperature is controlled at $20 \pm 1°$C. The experimental setup is sketched in Fig. 3. The tank is filled with the double-bucket technique using two drums, one initially filled with brine and the other with freshwater. The drums are filled with hot water to allow an efficient salt dissolution. A fixed volume of 10 mL of red food dye is added to the drum filled with brine. It is used as a passive tracer for salinity as described in the following subsection. The tank is filled to a height of $H \approx 27$ cm in approximately three hours using two floating devices. The slow flow rate allows a linear stratification to be obtained over the

fluid depth, while shallow mixed layers of less than 1 cm are observed close to the tank bottom and free surface, due to boundary exchanges. In most fills the two drums have been prepared 24 hours before the start of the fill to achieve temperature equilibrium between water and air. Several fills have been carried out with water hotter than air, which led to the formation of double diffusive layers. These layers had no visible impact on the internal wave dynamics and permitted observation of the interfacial displacement using the shadowgraph technique in qualitative experiments.

For most experiments, a constant Brunt-Väisälä frequency $N_0 = 0.7$ rad/s is set, with $N_0 = \sqrt{-g/\rho_0 \times d\bar{\rho}/dz}$. $g = 9.81$ m/s^2, $\rho_0 = 1000$ kg/m^3, $\bar{\rho}$ and z are the gravity, the reference density, the density profile and the vertical coordinate with the origin at the tank bottom, respectively. In total, 14 fills have been performed during the experimental campaign, for which the forcing parameters were varied.

The forcing is performed by towing a bidimensional ridge of Gaussian shape over the length of the tank, at the free surface of the fluid. The ridge profile is given by

$$h(x) = h_0 \exp\left(-\left(k_r x\right)^2\right), \tag{7}$$

where x is the horizontal coordinate with the origin at the center of the ridge base, $h_0 = 3.5$ cm is the ridge height and k_r is the characteric horizontal wavenumber. Experiments have been performed with three different ridges of varying e-folding width $l_r = 1/k_r = 1.5$ cm (ridge A), $l_r = 5$ cm (ridge B) and $l_r = 16$ cm (ridge C). The ridges are attached to a 80 cm long plate to allow for boundary layers to develop during motion. The weight of the plate is adjusted so that the ridge is completely submerged, and the flat section of the plate lies a few millimeters below the free surface. The ridge motion is controlled by a Smartmotor interface via a wire attached to a rotating cylinder.

The program independently controls a steady and an oscillatory rotation of the cylinder, which respectively impose a constant velocity U_c and an oscillatory velocity $U_0 \cos(\omega t)$ to the ridge. The ridge transits 1 to 20 times over the length of the tank during an experiment. The flow is decelerated/accelerated over 30 cms close to the end walls to ensure a continuous forcing velocity.

Hence, this configuration permits simulation of the combined effects of a geostrophic and a barotropic forcing interacting with an oceanic ridge. The relative magnitude of the two forcings as well as the tidal period can be adjusted to reach a parameter space relevant for oceanic configurations. The initially linear stratification represents the regular density gradient in the deep ocean.

Five selected experiments showing different aspects of the asymmetric generation of free beams - which are the main source of IW energy transport over hills apart from the Southern Ocean - are discussed in the following sections. Table 1 summarizes the relevant parameters of the experiments.

3.2. Light attenuation technique

The light attenuation technique infers local density from absorption measurements at high spatial resolution [*Allgayer and Hunt*, 1991; *Hacker et al.*, 1996; *Sutherland et al.*, 2012]. This method has previously been used to describe the dynamics of internal waves generated in the lee of a moving topography as well as the induced mixing [*Dossmann et al.*, 2016a].

The light absorption $A(x, z, t) = \log(I_0(x, z)/I(x, z, t)$ due to the red food dye is measured using the intensity field from a reference image ($I_0(x, z)$) and from an image recorded in the course of the experiment $I(x, z, t)$. The initial concentration of red dye is chosen

such the absorption law is in the linear (Beer-Lambert) regime: $A = \epsilon_\lambda W c$, where ϵ_r, W and c are the extinction coefficient for the red component of the camera sensor, the tank width and the dye concentration.

A calibration is applied using two density samples from the flow to eventually convert absorption values to cross-tank averaged density anomalies $\Delta\rho(x, z, t)$ at each pixel. A median filter is applied over 10 pixels in the two directions to remove measurement noise. The reader can refer to *Dossmann et al.* [2016a] for a detailed description of the light attenuation technique. A LED panel of dimensions 100 cm×60 cm is placed to illuminate to central part of the tank. Images are recorded in RAW format at 14 bits using a Nikon D300 DSLR camera equipped with a 200 mm telephoto lens. The camera is placed approximately 6 m away from the tank to minimize parallax effects.

4. Internal wave dynamics

In this section we investigate the dynamics induced by the flow/ridge interaction for varying the mean excursion distance parameter $\bar{\epsilon}$ and forcing frequency ω/N. In experiments II to V, the ridge is moving rightwards at a constant velocity $U_c = 2$ mm/s, which represents a leftwards steady flow. Hence the downstream (upstream) region is at the left (right) side of the ridge.

In the absence of the steady forcing flow ($\bar{\epsilon} = 0$) the generation of symmetrical internal wave beams on the two sides of the ridge is measured in experiment I. (Fig. 4). The beams are in phase opposition and their angle matches the expected angle from the linear dispersion relation. The high mode internal wave field is superimposed on a background wave field likely due to fast propagating low modes reflecting at the tank walls.

The steady flow is then turned on in experiment II ($\bar{\epsilon} = 0.09$), for the same ridge and forcing frequency as in experiment I (5). The generation of sharp beams occurs on both sides of the ridge with an important asymmetry between the upstream and downstream beams. The upstream beam shows a larger amplitude and is steeper than the downstream beam. The linear prediction of the beam angles including the steady flow is shown by the dashed lines in Fig. 5. Both beam angles match the linear dispersion relation. The slow rightwards ridge motion induces the periodic formation of a vortex on the lee side of the ridge as seen at $t = 0.71T$ (circled). This vortex only forms when the oscillatory and steady forcings are combined and is likely to contribute to mixing in the vicinity of the ridge.

Decreasing the ridge width in experiment III leads to a larger value of $\bar{\epsilon} = 0.36$ (see Fig. 6). Again sharp internal wave beams form periodically on the two sides of the ridge, with a larger angle difference between the upstream and downstreams beams than in experiment II. Contrary to experiment II, no vortex is observed close to the ridge. This indicates that the generation of this non-linear structure in the boundary layer is dependent on the shape of the topography.

The Doppler shift induced by the steady flow interacting with a sufficiently narrow ridge allows for the generation of a superbuoyancy IW beam in experiment IV ($\bar{\epsilon} = 0.20$ and $\omega/N = 1.21$, Fig. 6)). The propagating beam is generated on the downstream side on the ridge, while evanescent waves remain on the upstream side as predicted by the regime diagram in Fig. 1a. The superbuoyancy beam interferes with propagating subharmonic internal waves with a similar amplitude.

The asymmetry between the upstream and downstream dynamics is illustrated with on horizontal spacetime diagrams measured at mid-depth for exp II-IV in Fig. 8. The larger amplitude and shorter wavelength of the upstream beam are clearly visible in exps II-III. In exp IV, the periodic density anomalies do not propagate on the upstream side (as shown by the absence of slope in the spacetime diagram) while the subcritical downstream beam and a supercritical subharmonic beam propagate on the downstream side.

Finally, the ridge width is increased to the largest value of 16 cm in experiment V, while keeping the same steady velocity and forcing frequency as in exp I-III (Fig. 9). Hence the mean excursion parameter $\epsilon = 0.03$ is small relative to previous experiments and one expects a weak asymmetry between the downstream and upstream sides. In fact, periodic density anomalies with a horizontal scale comparable to l_r are generated by the ridge motion. These anomalies appear to be dominated by propagating low modes - by constrast with the sharper beams in exp I-IV. No asymmetry in the beams is measured in this experiment.

5. Energy Flux

The measured asymmetry between the upstream and downstream beams impacts the energy fluxes, $\mathbf{J}(x, z, t) = p\mathbf{v}$, carried by internal waves and eventually the induced mixing. The direct measure of energy fluxes remains an experimental challenge as it relies on the simultaneous measurements of the pressure and velocity fields. While it is possible to perform simultaneous measurements of velocity fields with other fields related to density and their derivatives to assess buoyancy fluxes, the authors are not aware of an experimental technique to directly measure the pressure anomaly field.

The method developed by *Allshouse et al.* [2016]; *Lee et al.* [2018] is applied to extract the linear energy flux radiated away by internal wave beams. In this method the pressure field is calculating from a Green's function method using the density anomaly field while the velocity field is obtained by integrating the continuity equation using the incompressibility assumption. This method was tested on experimental Schlieren data which provides density gradient fields that are then integrated to obtain density anomalies. Agreement with Navier-Stokes simulations was obtained for small-amplitude internal wave field. In the present work the density anomalies are directly measured from the light attenuation technique, which suppresses the spatial integration step. Instantaneous energy fluxes are calculated using the Matlab GUI EnergyFlux introduced by *Allshouse et al.* [2016]. Their mean contribution is post-processed and compared with the energy fluxes calculated from the extended linear theory described in 2.1 in Fig. 10.

When no steady flow is present, the energy flux is focussed in the symmetrical beams generated on either side of the ridge (exp I, Fig.10a. and d.). The predicted and experimental flux fields closely match in amplitude and direction. Adding a steady flow leads to an asymmetry in both the shape and the amplitudes of the energy carried away by the beams as described in section 4. In both experiments II ($\bar{\epsilon} = 0.36$, Fig10c. and f.) and III ($\bar{\epsilon} = 0.09$ Fig. 10b. and e.), the steady flow increases the energy flux in the upstream beam relative to the downstream beam. The experimental beam amplitudes are twice as large in exp II (ridge B) as in exp III (ridge C), showing the strong topographic control exerted by the ridge slope on the energy fluxes. The theoretical and experimental amplitudes are similar in the narrower ridge experiment III, however the linear energy fluxes are overestimated by a typical factor of 2 in exp II. A plausible explanation for

this overestimation is that other nonlinear processes are at play in exp II that lead to a saturation in the energy fluxes carried away by the linear IW beams. This explanation is consistent with the observation of a vertical vortex generated every tidal period in exp II (Fig. 5).

A visible beam doubling appears in both the predicted and experimental mean fluxes when measured in the Eulerian frame (exp II and III) owing to the relatively large value of the tidal excursion parameter. When measured in the co-tidal frame, the mean energy flux is focussed in a single beam as shown for exp I.

6. Discussion

The combination of a steady flow and an oscillatory flow impinging up on a topography leads to the generation of internal waves on both sides of the ridge in all selected experiments, except for exp IV in which the Doppler-shift prevents the generation of upstream internal waves. The latter case is one where downstream internal waves are 'flow-trapped' as they can only propagate in the presence of the steady flow [see the discussion of *Shakespeare*, 2020]. In experiments I, II, and III internal waves are organized as propagating 'free beams' that are modified by the steady flow but would still propagate if the steady flow is cancelled. These waves are asymmetric in their direction of propagation, their amplitude and their wavelength. The asymmetry is increased by increasing the magnitude of the steady flow and by decreasing the ridge width. The beam angles agree well with the extended dispersion relation, including a Doppler-shift, showing that these IWs propagate in a linear fashion. All experiments were performed in regimes where the internal wave field is dominated by propagating upstream and downstream beams relative to lee waves

owing to the small values of the steady flow. Hence, the signature of lee waves is not visible in the density anomalies, nor in the energy fluxes.

The processed energy flux fields are successfully compared against the extended linear theory described in section 2.1. The presence of a steady flow induces a larger amplitude and greater energy flux in the upstream beam compared with the downstream beam. The Doppler-shift leads to a more efficient barotropic to baroclinic conversion as the upstream beam approaches the near-critical regime described in *Dossmann et al.* [2011] while the downstream beam slope flattens. The measured asymmetry confirms the larger integrated energy fluxes measured on the upstream side of ocean ridges and consequently the existence of a net wave stress over abyssal hills proposed in *Shakespeare* [2020], noting that these experiments are performed in a limited framework compared with the ocean (non-rotating, single tidal forcing). Partial cancellation of the energy flux is expected when including multi-tidal forcing. Future experiments will focus on quantifying this cancellation by superimposing several tidal components in the oscillatory flow.

The steady flow amplitude is too weak to observe the generation of non-linear boundary layer structures (hydraulic jump, topographic blocking) described in *Dossmann et al.* [2016a]. However the coupling between the steady and oscillatory flows leads to the generation of periodic vortices that are likely to participate to mixing close to the topography and limit the energy transfer toward IW beams. The conditions for the generation of these vortices and their contribution to mixing relative to internal waves will be investigated in a companion experimental study.

The pathway to internal wave induced mixing in the ocean is likely to be affected by the coupling between the steady flow and the oscillatory flow. Internal wave mixing

processes are classified as either far-field or near-field, depending whether the internal wave energy escapes the generation site as propagating low-modes and dissipates elsewhere, or is dissipated in the vicinity of the topography through the breaking of higher mode internal waves. The various routes for far-field and near-field internal wave dissipation are reviewed by *MacKinnon et al.* [2017].

Low mode internal waves, generated by large scale topograpy (order 100 kms) are apparently unaffected by the presence of a steady flow, as illustrated in experiment V and consistent with theory predicting a weak Doppler shift at small wavenumber k_r. However, the remote breaking process of these waves involves a direct cascade of energy through scattering by topography, breaking at continental slopes, interactions with mesoscale steady flows and eddies *Dunphy and Lamb* [2014], and wave-wave interaction through Parametric Subharmonic Instability [*MacKinnon et al.*, 2013]. These mechanisms induce internal waves at larger wavenumber that can be subject to the Doppler shift in the presence of a steady flow or other tidal constituents. The role of the Doppler shift in the pathway to mixing for low mode internal tides is yet to be investigated.

For high mode internal waves generated at smaller scale abyssal hills of order 10 kms, the nearfield pathway to mixing is directly affected by the Doppler shift as seen in experiment II-IV. Several processes are likely to be involved in transfer of energy to the scales of mixing directly above the topography, such as interactions with a background internal wave field, convective instability *Buhler and Muller* [2009] and the PSI mechanism. The mixing efficiency of these mechanisms are controlled by the amplitude and wavenumber of the internal wave beams [*Joubaud et al.*, 2012; *Bourget et al.*, 2013]. In particular, the dominant sites for generation of high modes internal tides at abyssal hills are the mid-

ocean ridges in the Atlantic and western Indian Oceans. At these sites, the asymmetry is particularly favored by the combination of the large topographic roughness of order 10 kms, an efficient barotropic to baroclinic conversion of the M2 tide, and the existence of a steady flow. In fact, a global map of the mean excursion distance parameter shows that $\bar{\epsilon} \approx 0.1$ around mid-ocean ridges (Fig. 11), which is the range for asymmetric internal wave beam in the present experiments. The present work and *Shakespeare* [2020]) (their Fig. 11) suggest that nearfield diapycnal mixing processes are enhanced on the upstream side of abyssal hills. On the other hand, in regions where strong quasi-steady flows interact with abyssal roughness, as shown by the red patches in Fig. 11, the generation of lee waves is likely to be locally cancelled in specific areas due to the interaction with the M2 forcing flow as in the Drake Passage.

In recent works, new process dependent parameterizations of mixing have been proposed to represent the 3D distribution of mixing both in the near-field and in the far-field (relative to internal wave generation sites) using Lagrangian beam tracing from sources to sinks [*de Lavergne et al.*, 2019, 2020]. Four dissipative processes have been identified, including the generation of high mode internal waves at abyssal hills. Global maps of internal tide dissipation have been produced by summing the independent contributions of the three main tidal components (M2, S2 and K1). The coupling between these tidal constituents and with the steady flow is not accounted for but is likely to affect the geography of internal wave sources - by the partial energy transfers between different tidal components - and sinks - by modifying the path taken by internal wave beams to their breaking site. Consequently, the role played by the coupling process on the global distribution of mixing is a key property to investigate with the proposed parameterizations.

Acknowledgments.

This work was supported partly by the french PIA project Lorraine Université d' Excellence, reference ANR-15-IDEX-04-LUE. Yvan Dossmann acknowledges support from the Embassy of France in Australia. Reader can access the supporting data and linear model via an online repository [*Dossmann et al.*, 2020].

References

Aguilar, D. A., B. R. Sutherland, and D. J. Muraki (2006), Laboratory generation of internal waves from sinusoidal topography, *Deep Sea Research Part II: Topical Studies in Oceanography*, *53*(1-2), 96–115.

Allgayer, D. M., and G. R. Hunt (1991), On the application of the light-attenuation technique as a tool for non-intrusive buoyancy measurements, *Experimental Thermal and Fluid Science*, *38*, 257–261.

Allshouse, M. R., F. M. Lee, P. J. Morrison, and H. L. Swinney (2016), Internal wave pressure, velocity, and energy flux from density perturbations, *Physical Review Fluids*, *1*(1), 014,301.

Bell, T. H. (1975), Topographically generated internal waves in open ocean, *Journal of Geophysical Research*, *80*, 320–327.

Bourget, B., T. Dauxois, S. Joubaud, and P. Odier (2013), Experimental study of parametric subharmonic instability for internal plane waves, *Journal of Fluid Mechanics*, *723*, 1–20.

Buhler, O., and C. Muller (2009), Saturation of the Internal Tides and Induced Mixing in the Abyssal Ocean, *American Meteorological Society*, *39*.

Buijsman, M. C., J. M. Klymak, S. Legg, M. H. Alford, D. Farmer, J. A. MacKinnon, J. D. Nash, J.-H. Park, A. Pickering, and H. Simmons (2014), Three-dimensional double-ridge internal tide resonance in luzon strait, *Journal of Physical Oceanography*, *44*(3), 850–869.

de Lavergne, C., S. Falahat, G. Madec, F. Roquet, J. Nycander, and C. Vic (2019), Toward global maps of internal tide energy sinks, *Ocean Modelling*, *137*, 52–75.

de Lavergne, C., C. Vic, G. Madec, F. Roquet, A. F. Waterhouse, C. B. Whalen, Y. Cuypers, P. Bouruet Aubertot, B. Ferron, and T. Hibiya (2020), A Parameterization of Local and Remote Tidal Mixing, *Journal of Advances in Modeling Earth Systems*, *12*(5), e2020MS002,065.

Dossmann, Y., A. Paci, F. Auclair, and J. W. Floor (2011), Simultaneous velocity and density measurements for an energy-based approach to internal waves generated over a ridge, *Experiments in Fluids*, *51*(4), 1013–1028.

Dossmann, Y., M. G Rosevear, R. W. Griffiths, G. O. Hughes, M. Copeland, et al. (2016a), Experiments with mixing in stratified flow over a topographic ridge, *Journal of Geophysical Research: Oceans*, *121*(9), 6961–6977.

Dossmann, Y., B. Bourget, C. Brouzet, T. Dauxois, S. Joubaud, and P. Odier (2016b), Mixing by internal waves quantified using combined piv/plif technique, *Experiments in Fluids*, *57*(8), 132.

Dossmann, Y., C. Shakespeare, and A. M. Hogg (2020), Experimental data and linear model for "Asymmetric internal tide generation in the presence of a steady flow", doi: 10.5281/zenodo.3889612.

Dunphy, M., and K. G. Lamb (2014), Focusing and vertical mode scattering of the first mode internal tide by mesoscale eddy interaction, *Journal of Geophysical Research: Oceans*, *119*, 523–536.

Goff, J. A. (2010), Global prediction of abyssal hill root-mean-square heights from small-scale altimetric gravity variability, *Journal of Geophysical Research: Solid Earth*, *115*(B12).

Gregg, M. C., and E. Ozsoy (1999), Mixing on the black sea shelf north of the bosphorus, *Geophysical Research Letters*, *26*(13), 1869–1872.

Hacker, J., P. F. Linden, and S. B. Dalziel (1996), Mixing in lock-release gravity currents, *Dyn. Atmos Oceans*, *24*, 183–195.

Joubaud, S., J. Munroe, P. Odier, and T. Dauxois (2012), Experimental parametric subharmonic instability in stratified fluids, *Physics of Fluids*, *24*(4), 041703.

Kiss, A. E., A. M. Hogg, N. Hannah, F. Boeira Dias, G. B. Brassington, M. A. Chamberlain, C. Chapman, P. Dobrohotoff, C. M. Domingues, E. R. Duran, et al. (2020), Access-om2 v1. 0: a global ocean-sea ice model at three resolutions, *Geoscientific Model Development*, *13*(2), 401–442.

Lee, F. M., M. R. Allshouse, H. L. Swinney, and P. J. Morrison (2018), Internal wave energy flux from density perturbations in nonlinear stratifications, *Journal of Fluid Mechanics*, *856*, 898–920.

MacKinnon, J. A., M. H. Alford, O. Sun, R. Pinkel, Z. Zhao, and J. Klymak (2013), Parametric subharmonic instability of the internal tide at 29 n, *Journal of Physical Oceanography*, *43*(1), 17–28.

MacKinnon, J. A., Z. Zhao, C. B. Whalen, A. F. Waterhouse, D. S. Trossman, O. M. Sun, L. C. St. Laurent, H. L. Simmons, K. Polzin, R. Pinkel, et al. (2017), Climate process team on internal wave–driven ocean mixing, *Bulletin of the American Meteorological Society*, *98*(11), 2429–2454.

Melet, A., M. Nikurashin, C. Muller, S. Falahat, J. Nycander, P. G. Timko, B. K. Arbic, and J. A. Goff (2013a), Internal tide generation by abyssal hills using analytical theory, *Journal of Geophysical Research: Oceans*, *118*(11), 6303–6318.

Melet, A., R. Hallberg, S. Legg, and K. Polzin (2013b), Sensitivity of the ocean state to the vertical distribution of internal-tide-driven mixing, *Journal of Physical Oceanography*, *43*(3), 602–615.

Nikurashin, M., and R. Ferrari (2010a), Radiation and dissipation of internal waves generated by geostrophic motions impinging on small-scale topography: Theory, *Journal of Physical Oceanography*, *40*, 1055–1074.

Nikurashin, M., and R. Ferrari (2010b), Radiation and dissipation of internal waves generated by geostrophic motions impinging on small-scale topography: Application to the southern ocean, *Journal of Physical Oceanography*, *40*, 2025–2042.

Nikurashin, M., and R. Ferrari (2011), Global energy conversion rate from geostrophic flows into internal lee waves in the deep ocean, *Geophysical Research Letters*, *38*, L08,610.

Nikurashin, M., and R. Ferrari (2013), Global energy conversion rate from geostrophic flows into internal lee waves in the deep ocean, *Geophysical Research Letters*, *40*, 3133–3137.

513 Nycander, J. (2005), Generation of internal waves in the deep ocean by tides, *J. Geophys.*
514 *Res*, *110*, C10,028.
515 Nycander, J. (2006), Tidal generation of internal waves from a periodic array of steep
516 ridges, *Journal of Fluid Mechanics*, *567*, 415.
517 Polzin, K. L. (2009), An abyssal recipe, *Ocean Modelling*, *30*(4), 298–309.
518 Polzin, K. L., J. M. Toole, J. R. Ledwell, and R. W. Schmitt (1997), Spatial variability
519 of turbulent mixing in the abyssal ocean, *Science*, *276*(5309), 93–96.
520 Sarkar, S., and A. Scotti (2017), From topographic internal gravity waves to turbulence,
521 *Annual Review of Fluid Mechanics*, *49*, 195–220.
522 Shakespeare, C. J. (2020), Interdependence of internal tide and lee wave generation at
523 abyssal hills: global calculations, *Journal of Physical Oceanography*, *50*(3), 655–677.
524 Shakespeare, C. J., B. K. Arbic, and A. M. Hogg (2020a), The drag on the barotropic
525 tide due to baroclinic motions, *Journal of Physical Oceanography*, in review.
526 Shakespeare, C. J., A. F. Waterhouse, B. K. Arbic, A. M. Hogg, J. A. MacKinnon, and
527 H. L. Simmons (2020b), A simple model for dissipating and reflecting internal waves,
528 and its application to oceanographic observations, *Journal of Physical Oceanography*,
529 in review.
530 St. Laurent, L. C., H. L. Simmons, and S. R. Jayne (2002), Estimating tidally driven
531 mixing in the deep ocean, *Geophysical Research Letters*, *29*, 2106.
532 Sutherland, B. R., B. Lee, and J. K. Ansong (2012), Light attenuation experiments on
533 double diffusive plumes and fountains, *Physics of Fluids*, *24*, 066,605.
534 Todd, R. E. (2017), High-frequency internal waves and thick bottom mixed layers observed
535 by gliders in the gulf stream, *Geophysical Research Letters*, *44*(12), 6316–6325.

Yang, L., M. Nikurashin, A. M. Hogg, and B. M. Sloyan (2018), Energy loss from transient eddies due to lee wave generation in the southern ocean, *Journal of Physical Oceanography*, *48*(12), 2867–2885.

Zhang, H. P., B. King, and H. L. Swinney (2007), Experimental study of internal gravity waves generated by supercritical topography, *Physics of Fluids*, *19*(9), 096,602.

Zheng, K., and M. Nikurashin (2019), Downstream propagation and remote dissipation of internal waves in the southern ocean, *Journal of Physical Oceanography*, *49*(7), 1873–1887.

Exp	U_c (cm/s)	U_0 (cm/s)	ridge	ω/N	$\bar{\epsilon}$
I	0	2	B	0.66	0
II	0.2	2	B	0.66	0.09
III	0.2	2	A	0.70	0.36
IV	0.2	2	A	1.21	0.20
V	0.2	2	C	0.76	0.03

Table 1. Experimental parameters. The experiment is carried out several times to vary the duration of forcing sequences. The latter are separated by resting sequences to allow for measurements of the background stratification.

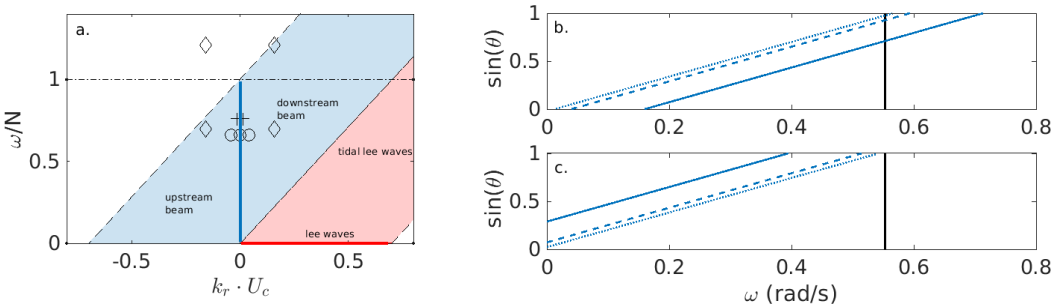

Figure 1. a. Regimes diagram for internal waves in the presence of an oscillatory and a steady forcing flow. The blue line and the blue shaded area are the non-evanescent bands for pure internal tides and free beams. The red line and the red shaded area are the non-evanescent bands for lee waves and tidal lee waves. The symbols ◊, ◯ and + show the experiments with ridge A, B and C, respectively.

b. and c. Linear dispersion relations for internal waves in the presence of a steady flow for the downstream (b) and upstream beams (c) for ridges A (solid), B (dashed) and C (dotted).

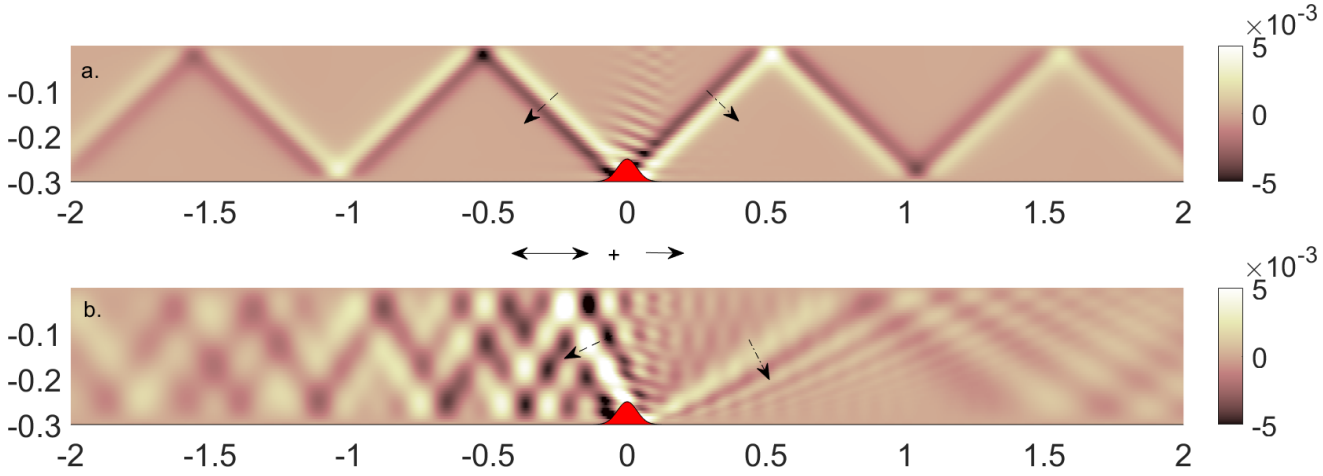

Figure 2. Vertical velocity (m/s) field for internal wave generation over a Gaussian ridge using the extended linear theory of *Bell* [1975] for independent (a.) and coupled (b.) forcings. The solid arrows show the relative magnitude of the oscillatory (2 cm/s) and steady (0,4 cm/s) flows. The dashed and dotted-dashed arrows indicate the phase propagation in the upstream and downstream beams. The topography is shown shaded in red.

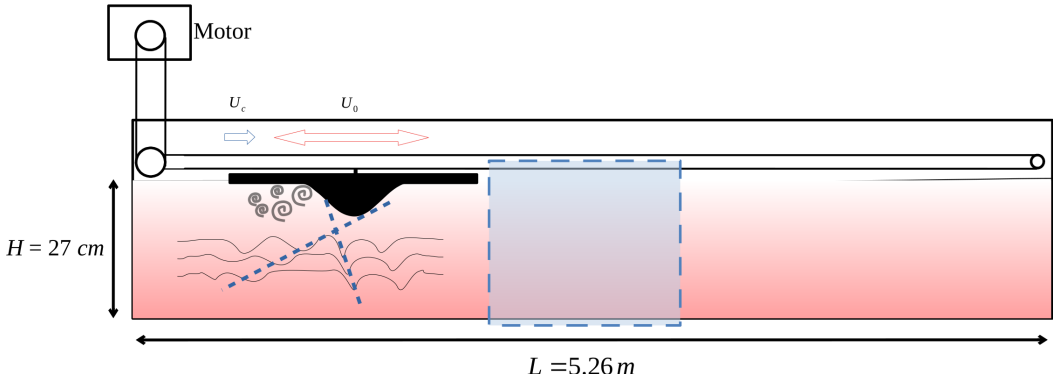

Figure 3. Sketch of the experimental apparatus. The tank is filled using the double-bucket technique with a linearly stratified fluid. The Step motor is computer-controlled to impose a steady (blue arrow) and oscillatory (red arrow) forcing motion to the ridge in Exps II-V, which generates internal wave beams in the body of the flow. The steady motion is set to zero in Exp I. The blue rectangle indicates the measurement area for the light attenuation technique.

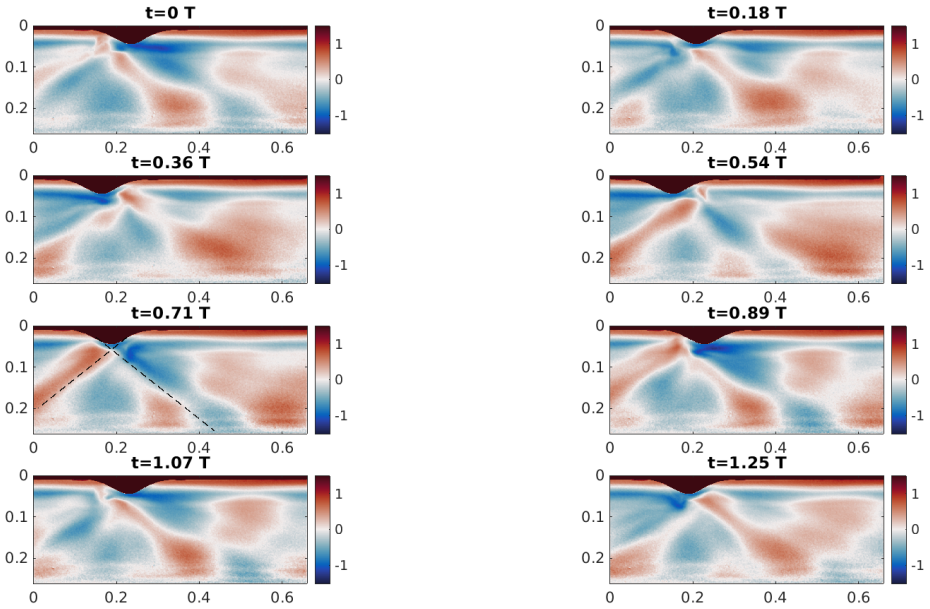

Figure 4. Exp I: Density anomaly field $\Delta\rho$ (kg/m)^3 ($U_c = 0$ cm/s, $U_0 = 2$ cm/s, $\omega/N = 0.66$, ridge B). The dashed lines show the beam angles predicted by linear theory.

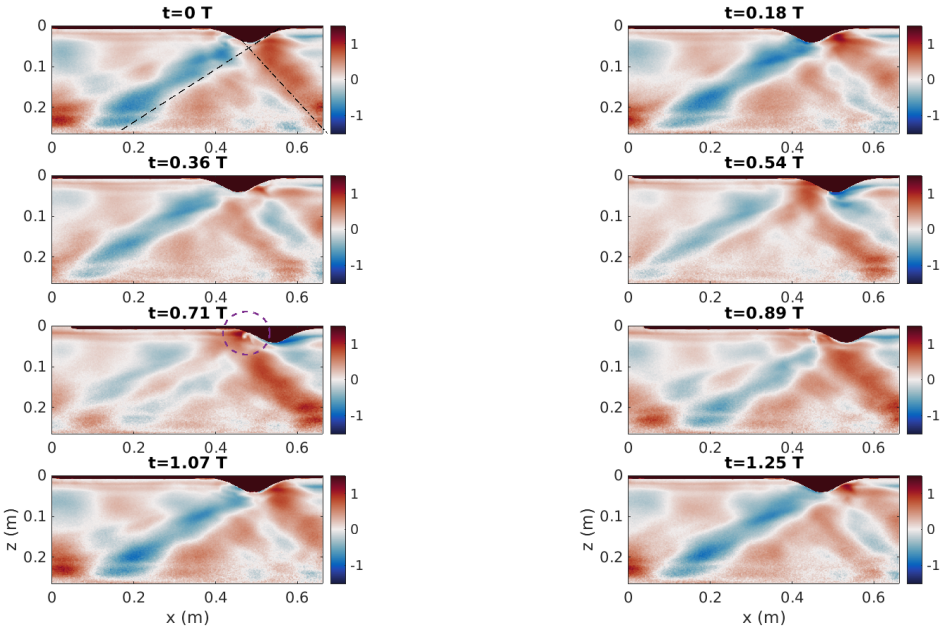

Figure 5. Exp II: Density anomaly field $\Delta\rho$ (kg/m)^3 ($U_c = 0.2$ cm/s, $U_0 = 2$ cm/s, $\omega/N = 0.66$, ridge B). The steady ridge motion is to the right of the field. The dashed lines show the beam angles predicted by linear theory. The formation of a vortex on the downstream side of the ridge is shown by the purple dashed circle at $t = 0.71$ T.

.

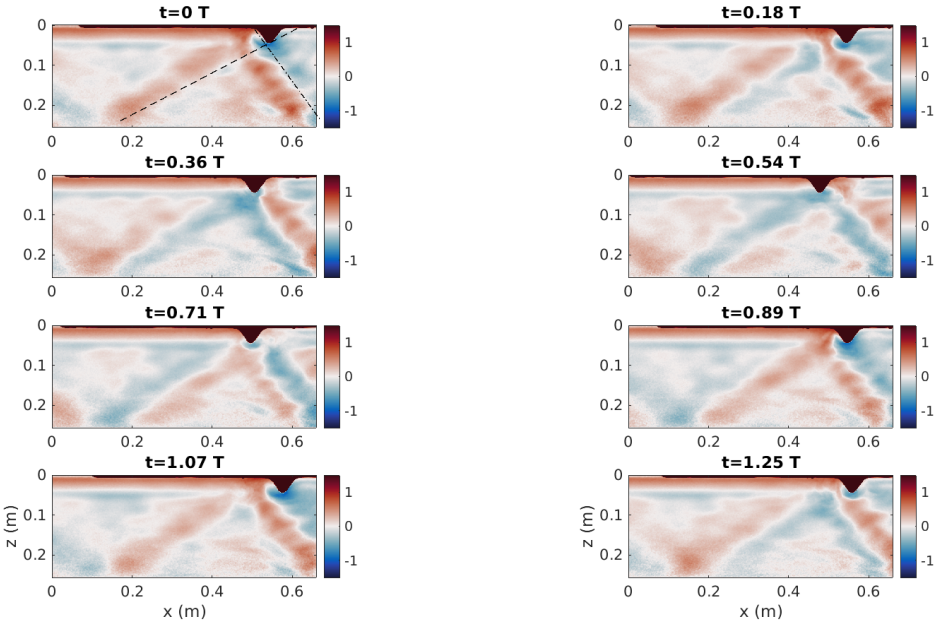

Figure 6. Exp III: Density anomaly field $\Delta\rho$ (kg/m)^3 (U_c = 0.2 cm/s, U_0 = 2 cm/s, $\omega/N = 0.70$, ridge A). The dashed lines show the beam angles predicted by linear theory.

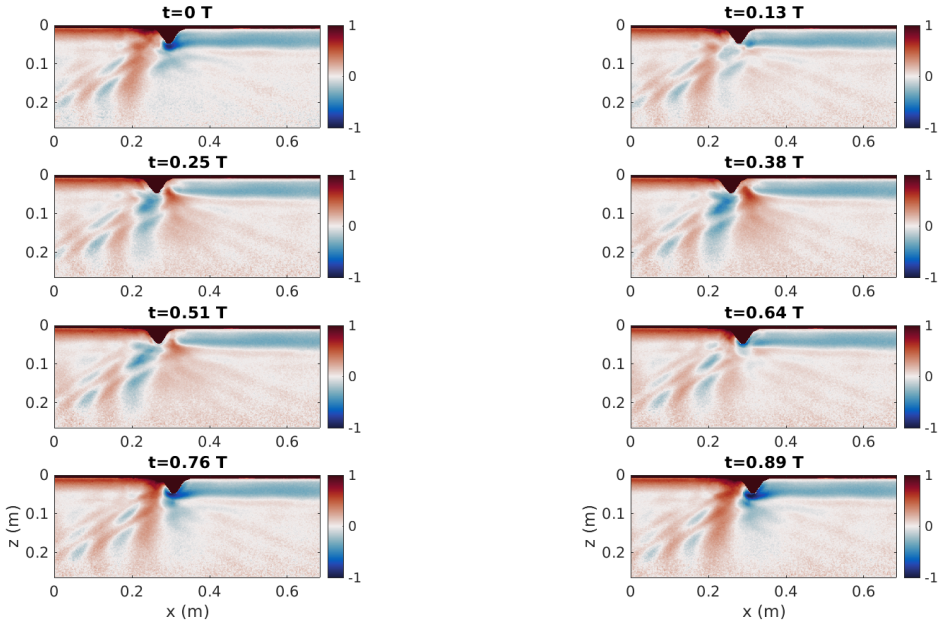

Figure 7. Exp IV: Density anomaly field $\Delta\rho$ (kg/m)^3 ($U_c = 0.2$ cm/s, $U_0 = 2$ cm/s, $\omega/N = 1.21$, ridge A).

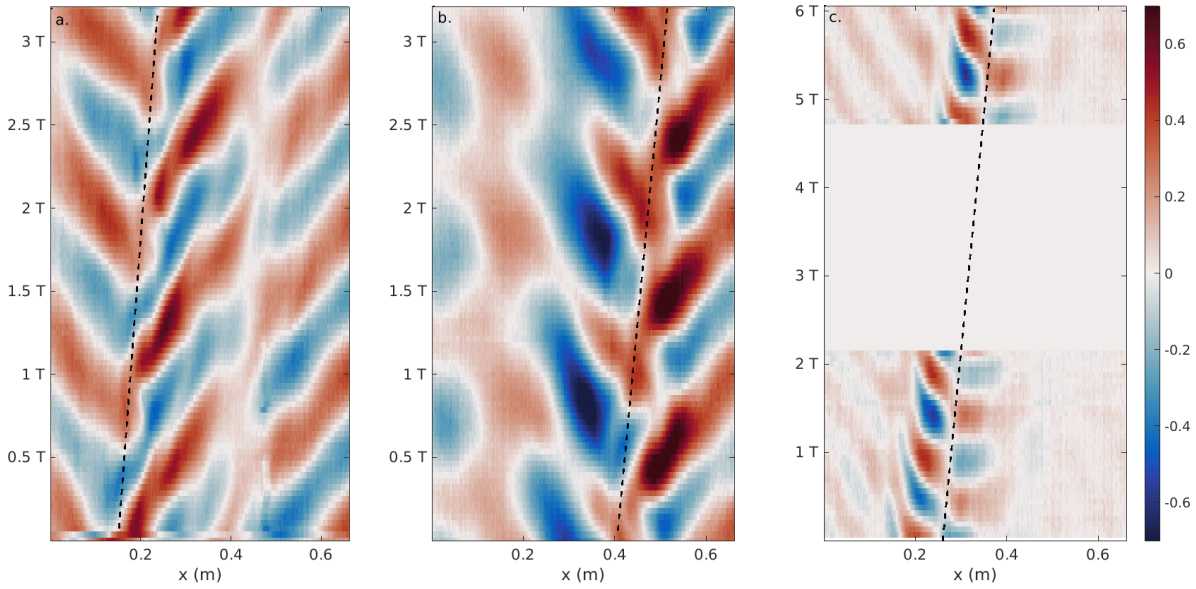

Figure 8. Density anomaly space-time diagrams at mid-depth for Exps III (a.), II (b.) and IV (c.). The dashed lines indicates the movement of the ridge due to the steady motion. The whitespace in (c) is where data are unavailable due to the limited camera buffer.

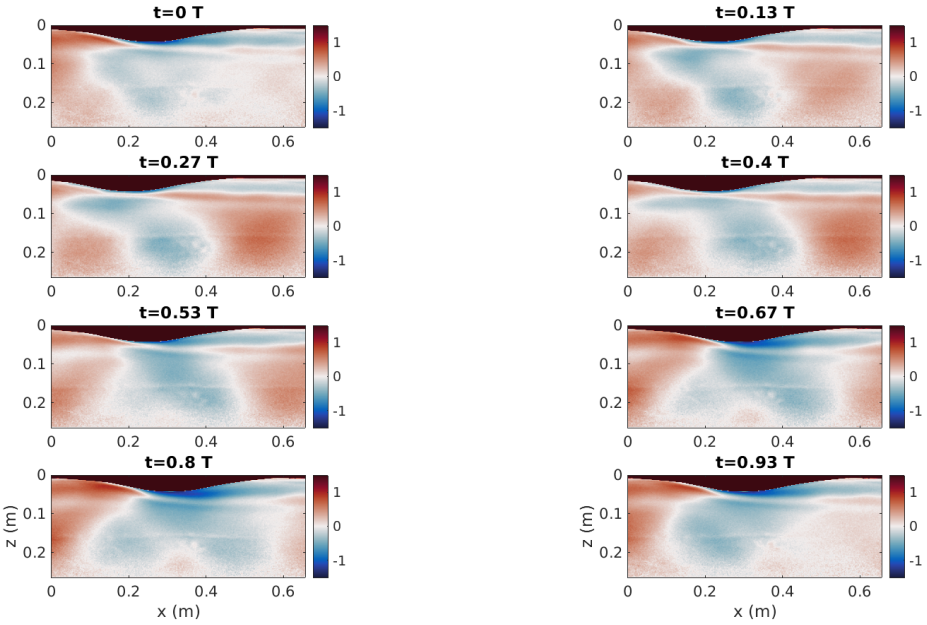

Figure 9. Exp V: Density anomaly field $\Delta\rho$ (kg/m)^3 ($U_c = 0.2$ cm/s, $U_o = 2$ cm/s, $\omega/N = 0.76$, ridge C).

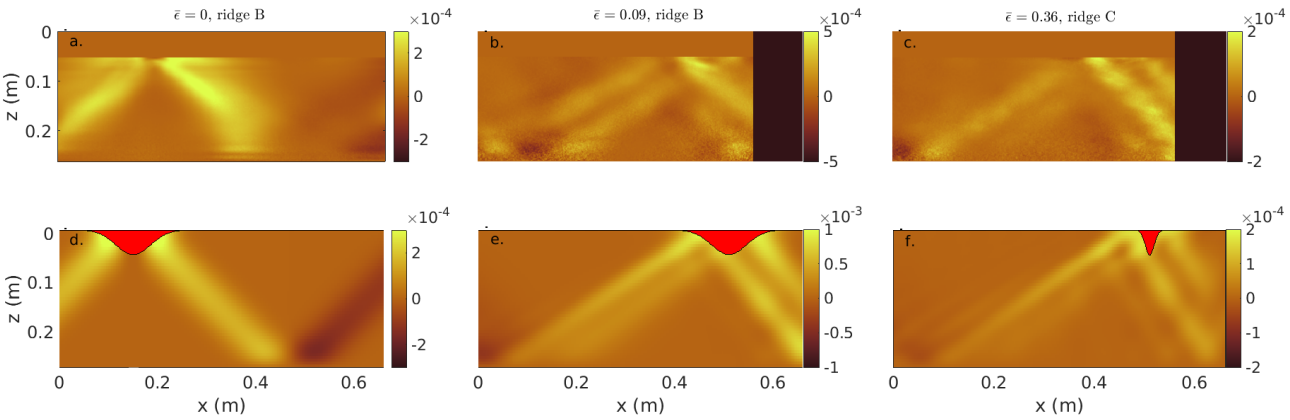

Figure 10. Mean energy fluxes measured in the experiments (top panels) and assessed from the extended Bell's theory (bottom panels) for Exp I (a, d), Exp II (b, e) and Exp III (c, f)

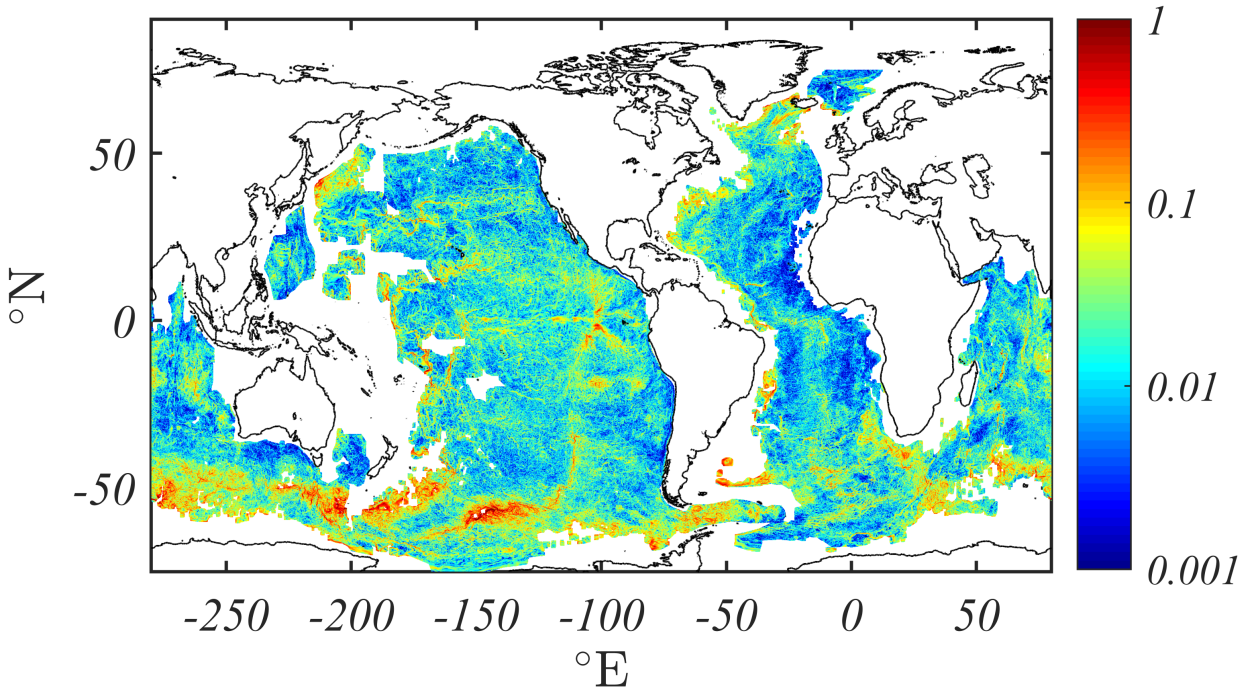

Figure 11. Mean excursion distance parameter $\bar{\epsilon} = k \times U_c/\omega_{M2}$ for the M2 tidal frequency, where k is the abyssal hill cut-off wavenumber. The steady near-bottom velocity U_c is obtained from 5-day averaged near-bottom velocities issued from the ACCESS-OM2-01 0.1^0 resolution global ocean-ice model [*Kiss et al.*, 2020]. Abyssal hill topography is sourced from *Goff* [2010]

.